Interaction-driven instabilities of a Dirac semimetal

C. Weeks and M. Franz
Department of Physics and Astronomy, University of British Columbia, Vancouver, British Columbia, Canada V6T 1Z1
(Received 20 October 2009; revised manuscript received 29 December 2009; published 5 February 2010)

We explore the possible particle-hole instabilities that can arise in a system of massless Dirac fermions on both the honeycomb and π-flux square lattices with short range interactions. Through analytical and numerical studies we show that these instabilities can result in a number of interesting phases. In addition to the previously identified charge and spin density wave phases and the exotic "quantum anomalous Hall" (Haldane) phase, we establish the existence of the dimerized "Kekulé" phase over a significant portion of the phase diagram and discuss the possibility of its spinful counterpart, the "spin Kekulé" phase. On the π-flux square lattice we also find various stripe phases, which do not occur on the honeycomb lattice. The Kekulé phase is described by a Z_3 order parameter whose singly quantized vortices carry fractional charge $\pm e/2$. On the π-flux lattice the analogous dimerized phase is described by a Z_4 order parameter. We perform a fully self-consistent calculation of the vortex structure inside the dimerized phase and find that close to the core the vortex resembles a familiar superconducting U(1) vortex, but at longer length scales a clear Z_4 structure emerges with domain walls along the lattice diagonals.

DOI: 10.1103/PhysRevB.81.085105 PACS number(s): 71.10.Fd, 73.20.−r

I. INTRODUCTION

Electrons hopping on the two-dimensional honeycomb lattice and the square lattice with a half magnetic flux quantum piercing each plaquette (π-flux lattice) exhibit, near half filling, a linearly dispersing excitation spectrum characteristic of massless Dirac fermions. The honeycomb lattice is realized in single layer graphene[1] while the π-flux square lattice has the potential to be realized in artificially engineered semiconductor heterostructures.[2] Such massless Dirac fermions exhibit a host of fascinating properties which underlie much of the current interest in graphene and the related systems.

Although Dirac fermions in graphene are intrinsically massless, it is interesting to contemplate the effects on its electronic properties of a band gap that would give rise to *massive* Dirac fermions. Experimentally, such a band gap can be realized by placing graphene on a specific substrate[3] that breaks the sublattice symmetry. Even more interesting is the possibility of the interaction-driven gap, resulting in a Mott insulating behavior. Aside from the conventional charge density wave (CDW) and spin density wave (SDW) instabilities, the structure of graphene allows for more interesting phases such as the quantum anomalous Hall (QAH) phase discussed by Haldane[4] and the quantum spin Hall (QSH) phase.[5,6] These phases are characterized by nontrivial topological invariants[7–9] and exhibit the quantum Hall effect in absence of magnetic field and the quantum spin-Hall effect, respectively. Although, as far as we know, these phases do not occur in natural graphene, the QSH phase was predicted to occur[10] and subsequently observed[11] in HgTe quantum wells. Also, theoretical studies of these phases led to the pioneering work on topological insulators in two and three spatial dimensions.[8,9,12,13]

Another interesting gapped phase on the honeycomb lattice is the Kekulé phase, illustrated in Fig. 1(b), which corresponds to a generalization of the dimerization pattern seen on the square lattice [Fig. 1(a)]. The Kekulé phase is topologically trivial but it is characterized by a Z_3 order parameter. The latter describes three degenerate Kekulé ground states, obtained by translating the pattern depicted in Fig. 1(b) by the Bravais lattice primitive vectors. Singly quantized vortices in the phase of this order parameter have been shown to possess a stable fermionic zero mode, carry fractional charge[14] $\pm e/2$, and obey fractional exchange statistics.[15,16] Similar physics is realized in the dimerized phase on the π-flux square lattice.[17]

In order to map out these interesting phases, Raghu *et al.*[18] studied a simple model describing fermions, both spinless and spinful, on the honeycomb lattice with short range interactions. They found phase diagrams containing CDW, SDW, QAH and QSH order but did not consider the possibility of the Kekulé phase. With the goal of complementing this previous work we study similar models and find

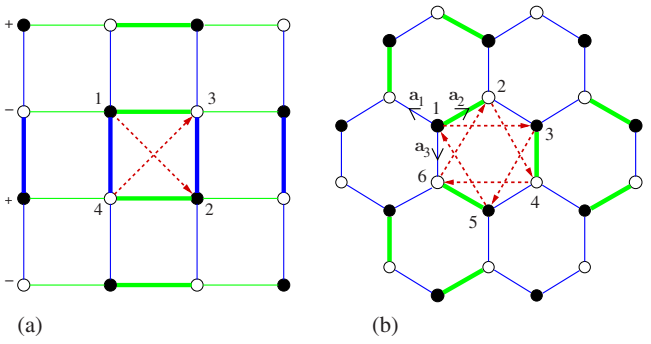

FIG. 1. (Color online) The model: (a) square lattice with $\frac{1}{2}\Phi_0$ magnetic flux per plaquette and dimerized hopping amplitudes. The $\pm$ on the left for each row show the choice of gauge for the Peierls phase factors. The thick (thin) bonds indicate an increased (decreased) hopping amplitude in the $\hat{x}$ and $\hat{y}$ directions, the ●/○ dots on the lattice sites represent an increase/decrease in local charge density, and the dotted red line indicates the NNN hopping (showing only inside a single plaquette). The four sites of the unit cell are marked 1–4. (b) Honeycomb lattice set up in analogous fashion with dimerized "Kekulé" phase, without magnetic field.

that the Kekulé phase is in fact present over a large portion of the phase diagram. Specifically, for spinless fermions, Kekulé order is established when the nearest-neighbor (NN) and next-nearest-neighbor (NNN) repulsion parameters V_1 and V_2 are of similar size. On the π-flux square lattice we obtain a phase diagram with the Kekulé phase replaced by a simpler dimerized phase having similar properties. In addition, we find stripe phases that tend to dominate over the QAH and the dimerized phases when V_2 is large. Nevertheless, when the third-neighbor repulsion V_3 is included, the Kekulé and QAH phases are stabilized over a portion of the phase diagram. For spinful fermions, the possibility of a novel spin-Kekulé phase characterized by the emergence of spatially modulated spin-dependent hopping amplitude is explored.

Having a mean-field theory of the dimerized phase for the π-flux model allows us to perform a self-consistent calculation of the electronic structure for a system having a vortex in the dimer order parameter, which is set up in a fashion similar to Ref. 17. The underlying Z_4 symmetry of the lattice raises the issue of whether it is realistic to talk of U(1) vortices in such a system, but as we have shown previously the fourfold anisotropy induced by the lattice is very weak and should support such vortices on length scales long compared to the lattice spacing. Further evidence is supplied here to support this claim.

II. SPINLESS FERMIONS

We begin with the tight-binding Hamiltonian for spinless fermions with NN and NNN interactions, $H=H_0+H_I$, with

$$H_0 = -t\sum_{\langle ij\rangle}(e^{i\theta_{ij}}c_i^\dagger c_j + \text{H.c.}), \tag{1}$$

and

$$H_I = V_1\sum_{\langle ij\rangle} n_i n_j + V_2\sum_{\langle\langle ij\rangle\rangle} n_i n_j. \tag{2}$$

Here $c_j^\dagger$ is the creation operator for a fermion on site $\mathbf{r}_j$ of the square or honeycomb lattice, the Peierls phase factor

$$\theta_{ij} = \frac{2\pi}{\Phi_0}\int_{\mathbf{r}_i}^{\mathbf{r}_j}\mathbf{A}\cdot d\mathbf{l} \tag{3}$$

is defined on a link $\langle ij\rangle$, t is the hopping amplitude between NN sites, V_1 and V_2 are the energy scales for NN and NNN interactions, respectively, and $n_i=c_i^\dagger c_i$ is the number operator. We focus on Hamiltonians H_0 that produce Dirac-type spectra for fermions in the absence of interactions.

In the following we treat H_I in the mean-field (MF) approximation which should provide reliable information about the possible gapped phases in the phase diagram. We consider both the on-site and bond MF decoupling channels,

$$n_i n_j \to n_i\langle n_j\rangle + n_j\langle n_i\rangle - \langle n_i\rangle\langle n_j\rangle, \tag{4}$$

$$n_i n_j \to -\Delta_{ij}c_i^\dagger c_j - \Delta_{ij}^* c_j^\dagger c_i + \Delta_{ij}\Delta_{ij}^*, \tag{5}$$

where $\Delta_{ij}=\langle c_j^\dagger c_i\rangle$ with i,j belonging to NN and NNN bonds.

A. π-flux square lattice

The system has a half magnetic flux quantum $\Phi_0=hc/e$ per plaquette. In this case the assumption of spinless fermions is quite natural because within the context of the realization described in Ref. 2 the electron spins would be polarized along the field. As in Ref. 17, we choose the Landau gauge $\mathbf{A}=(\Phi_0/2)(-y,0)$ where we have set the lattice spacing to unity and work at half filling. The unperturbed Hamiltonian then has a spectrum

$$E_{\mathbf{k}}^{(0)} = \pm 2t\sqrt{\sin^2 k_x + \cos^2 k_y}, \tag{6}$$

with Dirac points at $(0,\pm\pi/2)$. We note that although the position of the Dirac points in the Brillouin zone depends on the gauge all physical observables are gauge invariant.

The repulsive interactions can produce semimetal (SM), charge density wave (CDW), quantum anomalous Hall (QAH), stripe and dimerized phases. The unit cell for this set up has four basis sites and is displayed in Fig. 1(a). The SM phase corresponds to the undistorted π-flux lattice, which has no gap in the spectrum.

The CDW corresponds to a modulation in charge density in both the x and y directions resulting in a checkerboard pattern on the lattice, whereas the stripe phase will be modulated only along one direction, hence giving rise to "stripes" of increased/decreased charge density. We use the following ansatz:

$$\langle n_i\rangle = \frac{1}{2} + \rho(-1)^{i_x+i_y} + \nu(-1)^{i_x} \tag{7}$$

for these two phases where $\mathbf{r}_i=(i_x,i_y)$.

The QAH phase, which is characterized by a quantized Hall conductance without Landau levels, occurs when a gap opens due to the spontaneous breaking of time reversal invariance. We require here that its order parameter, $\Delta_{ij}=\Delta_{\hat{x}+\hat{y}}$, produces a NNN hopping consistent with a half-flux quantum per unit cell.

The dimerized phase, with its order parameter $\Delta_{ij}=\Delta_{\hat{x},\hat{y}}$ along NN this time, will act to increase/decrease the existing hopping amplitude t. It can nominally take on any value locally, but we concentrate on either constant dimerization or one that will support the quasi-$U(1)$ vortices mentioned above. We also note the energy scale t becomes isotropically renormalized for any finite value of V_1 yielding a contribution δt.

Introducing the Fourier transform, $c_j=N^{-1/2}\Sigma_{\mathbf{k}}e^{i\mathbf{k}\cdot\mathbf{r}_j}c_{\mathbf{k}}$, our Hamiltonian can then be brought into the matrix form in momentum space

$$H = \sum_{\mathbf{k}}\Psi_{\mathbf{k}}^\dagger\mathcal{H}_{\mathbf{k}}\Psi_{\mathbf{k}} + E_0, \tag{8}$$

where $\Psi_{\mathbf{k}}^\dagger=(c_{1\mathbf{k}}^\dagger,c_{2\mathbf{k}}^\dagger,c_{3\mathbf{k}}^\dagger,c_{4\mathbf{k}}^\dagger)$, and

$$E_0 = N\left[\frac{\bar{\rho}^2}{8(V_1-V_2-V_3)} + \frac{\bar{\nu}^2}{8(V_2-V_3)} + \frac{\eta_x^2+\eta_y^2}{V_1} + \frac{2}{V_2}\xi^2 + \frac{2}{V_1}\delta t^2\right], \tag{9}$$

with $\bar{\rho}=4\rho(V_2+V_3-V_1)$, $\bar{\nu}=4\nu(V_3-V_2)$, $\eta_x=V_1\Delta_{\hat{x}}$,

$\eta_y = V_1 \Delta_{\hat{y}}$, and $\xi = \Delta_{\hat{x}+\hat{y}} V_2$. The Hamiltonian matrix reads

$$\mathcal{H}_{\mathbf{k}} = \begin{pmatrix} \bar{\rho}+\bar{\nu} & \Gamma & \Omega_x & -\Omega_y^* \\ \Gamma^* & \bar{\rho}+\bar{\nu} & -\Omega_y & -\Omega_x^* \\ \Omega_x^* & -\Omega_y^* & -\bar{\rho}-\bar{\nu} & \Gamma \\ -\Omega_y & -\Omega_x & \Gamma^* & -\bar{\rho}-\bar{\nu} \end{pmatrix}, \tag{10}$$

with

$$\Omega_{x,y} = 2(\tilde{t}\cos k_{x,y} + i\eta_{x,y}\sin k_{x,y}), \tag{11}$$

$$\Gamma = 2i\xi[\cos(k_x + k_y) - \cos(k_y - k_x)] \tag{12}$$

and $\tilde{t} = t + \delta t$. For reasons that will become apparent shortly we have also included in the above analysis the third-nearest-neighbor (NNNN) repulsion V_3.

We can now diagonalize $\mathcal{H}_{\mathbf{k}}$ and obtain the exact dispersion (setting the chemical potential to zero) with four particle-hole symmetric branches

$$\begin{aligned} E_{\mathbf{k}} = \pm\{&\bar{\nu}^2 + \bar{\rho}^2 + 4\tilde{t}^2(c_x^2 + c_y^2) + 4(\eta_x^2 s_x^2 + \eta_y^2 s_y^2) \\ &+ 16\xi^2 s_x^2 s_y^2 \pm 2[\bar{\nu}^2\bar{\rho}^2 + 4\bar{\nu}^2\tilde{t}^2 c_y^2 - 32\bar{\nu}\tilde{t}\eta_x\xi c_y s_x^2 s_y \\ &+ 4\bar{\nu}^2\eta_y^2 s_y^2 + 16\bar{\rho}^2\xi^2 s_x^2 s_y^2 + 64\xi^2 s_x^2 s_y^2(\eta_x^2 s_x^2 + \eta_y^2 s_y^2)]^{1/2}\}^{1/2}. \end{aligned} \tag{13}$$

Here $\mathbf{k}$ is taken over the reduced Brillouin zone $-\frac{\pi}{2} \le k_x \le \frac{\pi}{2}$, $-\frac{\pi}{2} \le k_y \le \frac{\pi}{2}$ and $c_x = \cos k_x$, $s_y = \sin k_y$, etc.

From here, we may calculate the free energy

$$F = -\frac{1}{\beta}\sum_{\mathbf{k}} \ln(1 + e^{\beta E_{\mathbf{k}}}) + E_0, \tag{14}$$

where $\beta = 1/k_B T$ and the summation is over all four branches of $E_{\mathbf{k}}$. The ground state is then obtained by minimizing F with respect to each of the order parameters. This yields a set of gap equations (listed in Appendix, Sec. 1) from which the phase diagram (at $T=0$) seen in Fig. 2(a) below follows after a numerical self-consistent iteration. The transition from the SM phase to the CDW is second order, whereas all other transitions are first order.

We observe that, within the present model with V_1 and V_2, the stripe instability completely wipes out the QAH and the dimerized phases expected to occur at finite V_2. In order to suppress the stripe phase we include a further term in the Hamiltonian above, namely, a V_3 term for NNNN interactions. Such term will generically be present in any system that can support NN and NNN interactions. To simplify matters we shall ignore any contribution to the kinetic energy generated by V_3 and focus on the frustration it generates for the stripe instability. We find that for V_3 nonzero both the QAH and the dimerized phases are stabilized [Fig. 2(b)] although stripes reappear at stronger V_2.

B. Honeycomb lattice

On the honeycomb lattice we may set $\theta_{ij} = 0$ (no magnetic field needed for Dirac band structure). The unperturbed spectrum reads

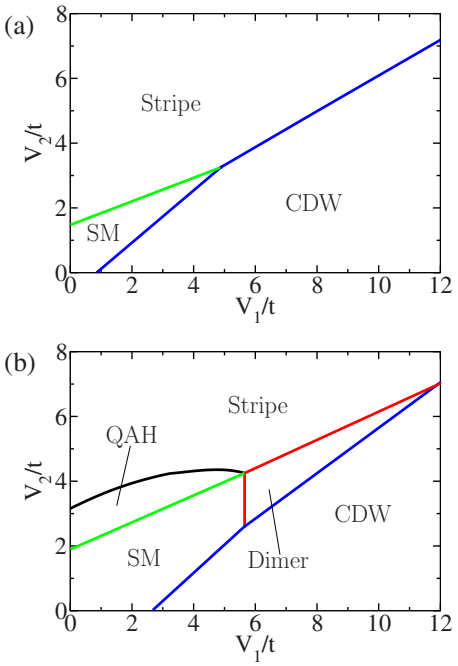

FIG. 2. (Color online) Phase diagram for π-flux model with spinless fermions. (a) $V_3 = 0$. (b) $V_3 = 1.5t$. (SM=Semimetal).

$$E_{\mathbf{k}}^{(0)} = \pm t|\tau(\mathbf{k})|, \tag{15}$$

where $\tau(\mathbf{k}) = \Sigma_i e^{i\mathbf{k}\cdot\mathbf{a}_i}$, with vectors $\mathbf{a}_i$ shown in Fig. 1(b). Also, there is no option of including a stripe phase, leaving us with the CDW, Kekulé, and QAH phases. As seen in Fig. 1(b) the system now has six atoms in the unit cell.

For the CDW we set

$$\rho = \frac{1}{2}(\langle n_i^A \rangle - \langle n_i^B \rangle), \tag{16}$$

where A and B refer to the two sublattices of the undistorted honeycomb lattice, which leads to the contribution (each site having three NN and six NNN sites)

$$\delta H_{\mathrm{CDW}} = 3\rho(V_1 - 2V_2)\sum_i n_i(-1)^i + \frac{3}{2}N\rho^2(V_1 - 2V_2). \tag{17}$$

For the Kekulé phase, we again use the decoupling in Eq. (4) where $c_i^\dagger c_j \langle c_j^\dagger c_i \rangle$ simply adds to the $t c_i^\dagger c_j$ term in H_0 according to

$$t \to t_a = t + \delta t + V_1 \eta_a, \quad a = 1,2,3 \tag{18}$$

and

$$\sum_{ij} V_{ij}\langle c_i^\dagger c_j\rangle\langle c_j^\dagger c_i\rangle = V_1(\eta_1^2 + \eta_2^2 + \eta_3^2)\frac{N}{2}. \tag{19}$$

The index a above labels the three bonds emanating from each A site. We may also write

$$\eta_a = \eta \cos\left(\varphi + \frac{2\pi}{3}a\right), \tag{20}$$

where φ parametrizes the most general Kekulé distortion. We shall find below that the ground-state energy is minimized by $\varphi=0,2\pi/3,4\pi/3$, corresponding to the three degenerate Kekulé ground states. For any φ it holds that $\Sigma_a \eta_a=0$ and $\Sigma_a \eta_a^2=\frac{3}{2}\eta^2$.

For the QAH phase we have $\langle c_i^\dagger c_j\rangle \equiv \xi_{ij}=\pm i\xi_\alpha$ (for $i,j\in$ NNN) where $\alpha=A,B$, and the sign is taken according to the arrow in Fig. 1(b). This generates a contribution

$$\delta H_{\mathrm{QAH}} = V_2 \sum_{\langle\langle ij\rangle\rangle} (\xi_{ij} c_i^\dagger c_j + \mathrm{H.c.}) + 3NV_2(\xi_A^2+\xi_B^2) \tag{21}$$

to the mean-field Hamiltonian.

Combining these contributions and Fourier transforming we arrive at the k-space Hamiltonian of the form Eq. (8) with $\Psi_{\mathbf{k}}$ a six-component spinor and

$$\mathcal{H}_{\mathbf{k}} = \begin{pmatrix} \bar{\rho} & \overline{\xi_A} S_{\mathbf{k}} & \overline{\xi_A} S_{\mathbf{k}}^* & t_3 e^{ik_1} & t_2 e^{ik_3} & t_1 e^{ik_2} \\ & \bar{\rho} & \overline{\xi_A} S_{\mathbf{k}} & t_2 e^{ik_2} & t_1 e^{ik_1} & t_3 e^{ik_3} \\ & & \bar{\rho} & t_1 e^{ik_3} & t_3 e^{ik_2} & t_2 e^{ik_1} \\ & & & -\bar{\rho} & -\overline{\xi_B} S_{\mathbf{k}} & -\overline{\xi_B} S_{\mathbf{k}}^* \\ & & & & -\bar{\rho} & -\overline{\xi_B} S_{\mathbf{k}} \\ & & & & & -\bar{\rho} \end{pmatrix}. \tag{22}$$

Here $\overline{\xi_\alpha}=\xi_\alpha V_2$, $\bar{\rho}=3\rho(V_1-2V_2)$, $k_i=\mathbf{a}_i\cdot\mathbf{k}$,

$$S_k = -i[e^{i(k_2-k_3)} + e^{i(k_3-k_1)} + e^{i(k_1-k_2)}], \tag{23}$$

and

$$E_0 = \frac{N}{2}\left[\frac{\bar{\rho}^2}{3(V_1-2V_2)} + \frac{\bar{\eta}^2}{V_1} + 3\frac{\overline{\xi_A}^2+\overline{\xi_B}^2}{V_2} + 3\frac{\delta t^2}{V_1}\right]. \tag{24}$$

The reduced Brillouin zone, which is derived below in the Appendix, Sec. 2, is comprised of the following set of points

$$(k_1,k_2,k_3) = \frac{2\pi}{3}\frac{1}{L}(n-m,m,-n), \tag{25}$$

where $m,n=1,2,\ldots,L$ and $6L^2=N$ is the total number of sites.

It is possible to find exact eigenvalues of the 6×6 matrix indicated in Eq. (22) by noticing that $\mathcal{H}_{\mathbf{k}}^2$ is block diagonal with two 3×3 blocks on the diagonal. Unfortunately, the eigenvalues obtained as roots of the associated cubic secular equations are given by lengthy and complicated expressions, which do not lend themselves to a convenient analysis. For this reason we choose to calculate the eigenvalues of $\mathcal{H}_{\mathbf{k}}$ numerically for a dense discrete set of momenta $\mathbf{k}$ in the first BZ. We use these eigenvalues to compute the free energy, Eq. (14), for a set of mean-field parameters $\bar{\rho}$, $\bar{\eta}$, φ, and $\bar{\xi}_\alpha$ and given fixed values of V_1 and V_2. The ground state of the system is then found by minimizing the free energy (at $T=0$) with respect to the above MF parameters. This is achieved by employing the standard Powel multivariate minimization routine.

The resulting phase diagram is displayed in Fig. 3. We observe that in addition to the CDW and QAH phases identified previously[18] a large portion of the phase diagram is occupied by the Kekulé phase.

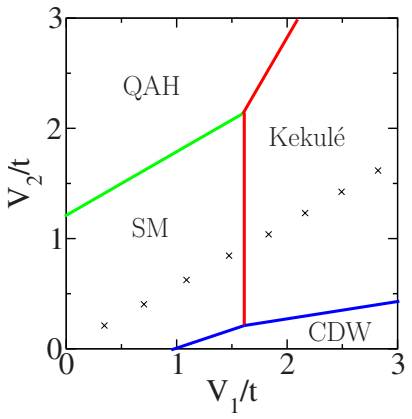

FIG. 3. (Color online) Phase diagram for honeycomb lattice. At the mean-field level all transitions from the SM phase are second order whereas transitions between all the gapped phases are first order. The ×'s represent the line along which the ratio V_2/V_1 would be expected to fall in graphene based on a crude estimate of the bare Coulomb repulsion (Ref. 19).

Although the critical lines in the phase diagram are determined numerically, the critical couplings for the CDW at $V_2=0$ and for QAH at $V_1=0$ can be found exactly from the corresponding gap equations for the model excluding Kekulé order. These read

$$\frac{\tilde{t}}{V_{1c}} = \frac{3}{N}\sum_{\mathbf{k}} \frac{1}{|\tau(\mathbf{k})|} \simeq 1.341, \tag{26}$$

$$\frac{\tilde{t}}{V_{2c}} = \frac{2}{3N}\sum_{\mathbf{k}} \frac{\left(\sum_i \sin \mathbf{k}\cdot\mathbf{b}_i\right)^2}{|\tau(\mathbf{k})|} \simeq 0.840, \tag{27}$$

where the $\mathbf{b}_i$ correspond to the set of NNN vectors for either of the triangular sublattices inside a single plaquette. If we wish to express critical couplings in terms of the bare hopping amplitude t we must include the MF equation for the hopping renormalization

$$\delta t = V_1 \frac{1}{3N}\sum_{\mathbf{k}} |\tau(\mathbf{k})| \simeq 0.262 V_1. \tag{28}$$

We thus obtain $V_{1c}\simeq 0.93t$ and $V_{2c}\simeq 1.20t$, in good agreement with the numerical results of Fig. 3. Our value of V_{2c} also agrees with Ref. 18, but our V_{1c} is smaller by a factor of about 1.5 when expressed in terms of t and about a factor of 2 in terms $\tilde{t}$. We do not know what is the reason for this discrepancy. Since the critical couplings quoted above agree with our numerically determined phase diagram, we are confident that these are correct within the definitions employed in this study.

III. SELF-CONSISTENT VORTEX STRUCTURE

In a superconductor or a superfluid the order parameter has a global U(1) symmetry related to its complex phase.

This means that, even on a lattice, a U(1) vortex is a legitimate topological defect. In the Kekulé (dimerized) phase the order parameter exhibits a global Z_3 (Z_4) symmetry leading to the possibility of a Z_3 (Z_4) vortex, which can be pictured as a point where the corresponding 3 (4) domains meet. Since the domain walls cost an energy per unit length, the energy of a single isolated Z_n vortex diverges linearly with the system size and, equivalently, a vortex-antivortex pair experiences linear confinement. U(1) vortices, on the other hand, experience only logarithmic confinement. This has important consequences for the appearance of vortices in these systems. U(1) vortices can thermally unbind above the Kosterlitz-Thouless transition temperature T_{KT} while Z_n vortices remain confined at all temperatures.

It has been suggested[17] that the Z_n vortices in the Kekulé or dimerized phase can nevertheless be observed since at short length scales they resemble U(1) vortices, and thus, for relatively short intervortex separations, interact only logarithmically. This has to do with the fact that the energy cost of a domain wall is relatively small. At length scales exceeding the confinement length ζ_{conf}, vortices remain linearly confined, as dictated by symmetry. If ζ_{conf} is sufficiently long compared to the vortex core size ζ_v, however, then the zero mode and the fractional charge associated with an individual vortex could be observed experimentally. To address this issue quantitatively we now carry out a fully self-consistent calculation of a vortex in the dimerized phase on the π-flux lattice. Our calculations show that, indeed, at short length scales, a vortex in the dimer order parameter resembles a U(1) vortex while on longer length scales clear domains separated by domain walls emerge.

Within our region of parameter space on the square lattice having a stable dimerized phase, we set up a discretized version of a U(1) vortex in the dimerization pattern Δ_{ij} as described in Ref. 17. For this initial vortex the corresponding MF Hamiltonian

$$H_{\text{MF}} = H_0 + \sum_{\langle ij \rangle} (\Delta_{ij} c_i^\dagger c_j + \text{H.c.}) \tag{29}$$

is diagonalized and the new order parameter is found using the condition

$$\Delta_{ij} = \langle c_i^\dagger c_j \rangle = U_{li}^\dagger U_{jk} \langle d_l^\dagger d_k \rangle = \sum_l U_{li}^\dagger U_{jl} f(\epsilon_l), \tag{30}$$

where f is the Fermi function, and ϵ_l and d_j are the eigenvalues and the eigenmodes of H_{MF}. The unitary matrices U_{ij} are comprised of the eigenvectors of the corresponding Hamiltonian matrix $\mathcal{H}_{ij}$, which we find numerically through exact diagonalization. Equations (29) and (30) are then iterated to self-consistency. We have solved the system for odd lattice sizes up to 49×49 using open boundary conditions with a vortex positioned at the central site.

Our results for the self-consistent vortex structure are summarized in Fig. 4. Instead of (real) bond fields Δ_{ij} it is useful to consider a complex on-site "dimer" order parameter defined as

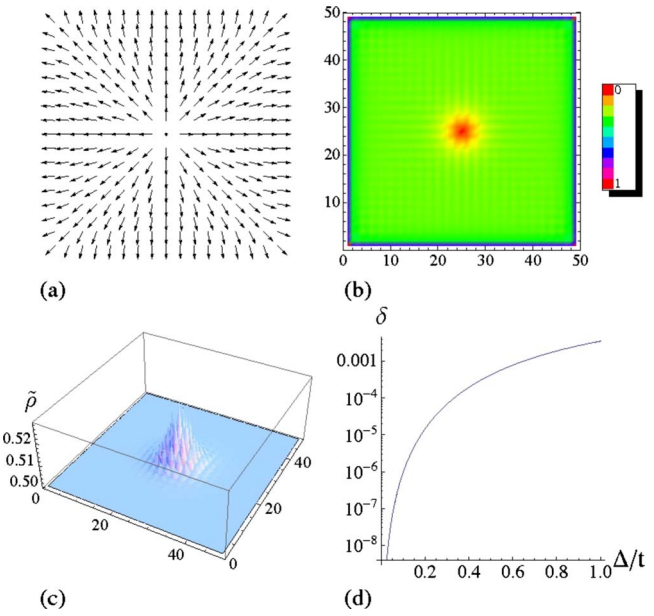

FIG. 4. (Color online) Self-consistent vortex structure in the dimerized phase. (a) Phase and (b) magnitude of the on-site dimer order parameter g_i defined in Eq. (31). (c) Charge density profile showing excess charge density in the vortex core. The total accumulated charge is $e/2$. (d) Anisotropy parameter δ defined in Eq. (35). For figures (a)–(c), $\Delta/t \approx 0.24$.

$$g_i = e^{i\pi/4} \sum_{\hat{\mu}} \gamma_{i,i+\hat{\mu}} \Delta_{i,i+\hat{\mu}}. \tag{31}$$

Here the $\hat{\mu}$ are the four nearest-neighbor unit vectors, $\gamma_{i,i+\hat{x}} = (-1)^{i_x}$, $\gamma_{i,i+\hat{y}} = \imath(-1)^{i_y}$, and $\gamma_{i,i-\hat{\mu}} = \gamma_{i-\hat{\mu},i}$. The phase of g_i contains information on the local orientation of the dimer pattern, e.g., $g_i \sim e^{i(\pi/2)[n-(1/2)]}$ with $n = 1,2,3,4$ describes four basic "columnar" patterns modulated along the x and y directions while $g_i \sim e^{i(\pi/2)n}$ describes four possible 'box' phases with the strength of dimerization modulated along both the x and y directions. We note that in the uniform system the box phases correspond to the ground states.

The vortex has a finite size core with a radius inversely proportional to the gap Δ, as seen in Fig. 4(b). Near the core the phase behaves as in a U(1) vortex although at longer distances domain walls are seen to form along the lattice diagonals, Fig. 4(a), characteristic of a Z_4 vortex. If we plot the charge density, $\tilde{\rho}_i = e\langle n_i \rangle$, over the lattice, where $\langle n_i \rangle$ is the average occupation number on site i, a net fractional charge $e/2$ accumulates near the core, Fig. 4(c), as expected on the basis of general arguments.[14,17]

The nature of the dimerized box ground state and the competition with other possible states can be understood from the following analysis. If we tune V_1 and V_2 so that we are in the dimerized phase, then all other order parameters can be set to zero. In the uniform state we can parameterize η_x and η_y by an angle χ, so that $\boldsymbol{\Delta} = (\eta_x, \eta_y) = \Delta(\cos\chi, \sin\chi)$, and write our ground state energy per site as (summing over all negative energy states)

$$E_0(\chi) = -\sum_{\mathbf{k}} \sqrt{\epsilon_{\mathbf{k}}^2 + \omega_{\mathbf{k}}^2}, \tag{32}$$

with

$$\epsilon_{\mathbf{k}}^2 = 4t^2(\cos^2 k_x + \cos^2 k_y) + \frac{\Delta^2}{2}(\sin^2 k_x + \sin^2 k_y),$$

$$\omega_{\mathbf{k}}^2 = \frac{\Delta^2}{2}\cos 2\chi(\sin^2 k_x - \sin^2 k_y).$$

Taylor expanding

$$\epsilon_{\mathbf{k}}\sqrt{1+\frac{\omega_{\mathbf{k}}^2}{\epsilon_{\mathbf{k}}^2}} \simeq \epsilon_{\mathbf{k}}\left(1+\frac{1}{2}\frac{\omega_{\mathbf{k}}^2}{\epsilon_{\mathbf{k}}^2}-\frac{1}{8}\frac{\omega_{\mathbf{k}}^4}{\epsilon_{\mathbf{k}}^4}\right) \tag{33}$$

we then have to fourth order in $\omega_{\mathbf{k}}$

$$E_0(\chi) = -\sum_{\mathbf{k}} \epsilon_{\mathbf{k}} + \frac{\Delta^4}{32}\cos^2 2\chi \sum_{\mathbf{k}} \frac{(\sin^2 k_x - \sin^2 k_y)^2}{\epsilon_{\mathbf{k}}^3}. \tag{34}$$

The ground state is clearly minimized by $\chi = \pm\frac{n\pi}{4}$ for $n=1,3$, corresponding to the box phase. The columnar phase corresponds to the maximum of energy. However, by plotting the anisotropy ratio

$$\delta = \frac{E_0(0) - E_0(\pi/4)}{E_0(\pi/4)} \tag{35}$$

against Δ/t, one can see, as in Fig. 4(d), that the difference between the maximum and minimum values of $E_0(\chi)$ will be very small for a broad range of values of Δ/t. The smallness of δ explains why at short length scales our Z_4 vortex behaves as a U(1) vortex.

IV. SPINFUL FERMIONS

For spinful Fermions a Hubbard term $U\Sigma_i n_{i\uparrow} n_{i\downarrow}$ must be added to the interaction Hamiltonian, Eq. (2), reflecting the strong on-site Coulomb repulsion between electrons of opposite spin. It is well known that for a bipartite lattice, a large U favors the antiferromagnetic SDW state. The mean-field phase diagram for spinful electrons on the honeycomb lattice in the U-V_1-V_2 space has been mapped out in Ref. 18, disregarding however the Kekulé phase. Our studies in the spinless case suggest that when V_1 and V_2 are comparable and much larger than U then a Kekulé phase will emerge in the spinful case as well, and can be thought of simply as the Kekulé phase for spin up and down electrons. We have verified that for small values of U the phase diagram in the spinful case resembles that shown in Fig. 3 except that the QAH phase is replaced by the QSH phase.[18] The two are degenerate at the mean-field level but quantum fluctuations favor the latter.

A question that we would like to answer here is whether there exist any new Kekulé-like phases in the spinful case. Specifically we considered a "spin Kekulé" phase whose order parameter is defined as follows. The nearest-neighbor interactions in H_I can be rewritten using the identity $(n_i-1)(n_j-1) = 1-\frac{1}{2}(\chi_{ij}^{\mu})^{\dagger}\chi_{ij}^{\mu}$, where $\chi_{ij}^{\mu} = c_{i\alpha}^{\dagger}\sigma_{\alpha\beta}^{\mu}c_{j\beta}$, $\mu=0,\ldots,3$, and $\sigma^{\mu}=(1,\sigma)$. In a mean-field picture, then, $\langle\chi^0\rangle \neq 0$ corresponds to the standard Kekulé phase and $\langle\chi^i\rangle \neq 0$ describes the spinful version.

We find, however, that the spin Kekulé phase is not a mean-field ground state of our Hamiltonian. Instead, a state in which two projections of the spin form the ordinary Kekulé phase is favored. This can be seen from the following symmetry based argument. We focus on the $\mu=3$ state and put the spin up into the ordinary Kekulé phase with parameters (η,φ) that minimize its ground state energy. The spin down electrons must then go into the Kekulé phase with parameters $(-\eta,\varphi)$ due to the σ_3 in the order parameter. However, this is not a ground state for spin down electrons, meaning that the overall energy must be higher than the $\mu=0$ state. Thus the energy of the SK phase is not exactly degenerate with the standard Kekulé phase as is the case for the QAH/QSH spectrum, but instead has a small splitting with the Kekulé phase being favored as the ground state. So, in absence of some type of interaction that could favor the SK phases, our current Hamiltonian is not capable of producing this potentially interesting phase.

Mapping out the complete phase diagram for the spinful electrons including the Kekule-type phases is a daunting task that we leave to a future investigation. The number of possible mean-field order parameters becomes large and the already complicated Hamiltonian in Eq. (22) becomes a 12×12 matrix. However, several observations can be made without detailed calculations: (i) starting from the phase diagram Fig. 3 (corresponding to $U=0$) one may track the fate of various phases as U is increased. (ii) It is clear that all the phases will persist for a range of values of U but will be replaced by a SDW when U exceeds a critical value. The transition from the SM phase will be second order while the transitions from the gapped phases will be first order. (iii) When $V_1 \ll V_2$ or $V_1 \gg V_2$ the phase diagram will be the same as that found in Ref. 18, because the Kekulé phase is stabilized when V_1 and V_2 are of similar magnitude.

V. CONCLUSIONS

Our studies show that interacting fermions moving on the honeycomb and π-flux square lattices can form a stable Kekulé phase, in addition to the previously identified CDW, SDW, and QAH/QSH phases. Two questions naturally arise: can the Kekulé phase be stabilized in a realistic system, and if so, how can it be experimentally observed? Inspection of the phase diagram shown in Fig. 2 reveals that the prospects of observing the Kekulé (dimerized) phase on the square lattice are not very good. When the NNN interaction is sufficiently strong to suppress the CDW, one obtains the stripe phase. Even when this is suppressed by introduction of NNNN repulsion, the dimerized phase appears only at strong coupling ($V_1 \simeq 6t$) and only in a small sliver of the parameter space. We thus conclude that although the square lattice is very convenient from the point of view of theoretical considerations, it is an unlikely candidate for the experimental observation of the dimerized phase.

Prospects for the Kekulé phase appear much better on the honeycomb lattice as it occupies a large portion of the V_1-V_2 mean-field phase diagram shown in Fig. 3. The Kekulé phase should appear whenever the interaction strength becomes large and V_1 and V_2 are comparable. In natural graphene the

Coulomb interaction is strong but evidently not strong enough to open up a gap at the Dirac point,[1] at least when a sample is placed on a substrate such as SiO_2. It has been suggested recently, on the basis of large scale Monte Carlo simulations, that graphene freely suspended *in vacuum* could become an insulator when the Coulomb interaction between electrons is accounted for.[19] The difference between the substrate and vacuum arises from the dielectric constant, which weakens the Coulomb interaction in the vicinity of a polarizable solid such as SiO_2, and also because of disorder induced by the substrate. Although Ref. 19 focused on the CDW instability, one may argue based on our present mean-field study that the Kekulé phase is a more likely candidate for an instability induced by the Coulomb interaction. In a very crude estimate the ratio V_2/V_1 should be equal to the ratio between the NN and NNN bond lengths, i.e., $V_2/V_1 \approx 1/\sqrt{3} \simeq 0.5773$. As illustrated in Fig. 3, this ratio of V_2/V_1 clearly favors the Kekulé phase over CDW if the overall effective interaction strength is strong enough to open up a gap. Recent experimental observation of the fractional quantum Hall effect in suspended graphene[20] confirms the increased importance of interactions over graphene on a substrate, where the fractional quantum Hall effect thus far eluded experimental detection. At zero field, however, even the suspended samples appear semimetallic[20] down to 1.2 K, suggesting that Coulomb interactions are still too weak to open up a significant gap. We note, finally, that the Kekulé phase has been proposed to emerge as the leading instability of graphene in an applied magnetic field.[21] Also, a phase analogous to the Kekulé phase in graphene has been proposed to exist for electrons on the kagome lattice at 1/3 filling.[22]

The Kekulé phase has broken translational symmetry characterized by a wave vector connecting the two inequivalent Dirac points in the graphene spectrum. The on-site charge density remains uniform and this limits the spectrum of experimental probes capable of detecting this pattern of symmetry breaking. Here we propose to use the technique of Fourier transform scanning tunneling spectroscopy (FT-STS) that has already been applied to graphene.[23] With sufficient resolution, FT-STS allows the mapping out of fine details of quasiparticle interference patterns at nonzero momenta, and, with help from the theoretical modeling of such patterns,[24] it should be possible to establish the existence of the Kekulé or other symmetry breaking phases.

ACKNOWLEDGMENTS

The authors have benefited from discussions with B. Seradjeh and G. Semenoff. This work was supported by NSERC, CIfAR, and the Aspen Center of Physics.

APPENDIX

1. Gap equations

For completeness we list the gap equations for the π-flux model on the square lattice in the limit $T \to 0$ for $\bar{\nu}$, $\bar{\rho}$, η_x, η_y, ξ, and δt,

$$\bar{\rho} = \frac{4(V_1 - V_2 - V_3)}{N} \sum_{\mathbf{k},\pm} \frac{1}{|E_{k,\pm}|} \left[\bar{\rho} \pm \frac{1}{\tilde{E}_k} (\bar{\nu}^2 \bar{\rho} + 16 \bar{\rho} \xi^2 \sin^2 k_x \sin^2 k_y) \right], \tag{A1}$$

$$\bar{\nu} = \frac{4(V_2 - V_3)}{N} \sum_{k,\pm} \frac{1}{|E_{k,\pm}|} \left[\bar{\nu} \pm \frac{1}{\tilde{E}_k} (\bar{\nu}\bar{\rho}^2 + 4\bar{\nu}\tilde{t}^2 \cos^2 k_y - 16 \eta_x \xi \cos k_y \sin^2 k_x \sin k_y + 4 \bar{\nu} \eta_y^2 \sin^2 k_y) \right], \tag{A2}$$

$$\eta_x = \frac{2V_1}{N} \sum_{k,\pm} \frac{1}{|E_{k,\pm}|} \times \left[\eta_x \sin^2 k_x \pm \frac{1}{\tilde{E}_k} \sin^2 k_x (16 \xi^2 \eta_x \sin^2 k_x \sin^2 k_y - 4 \bar{\nu} \tilde{t} \xi \cos k_y \sin k_y) \right], \tag{A3}$$

$$\eta_y = \frac{2V_1}{N} \sum_{k,\pm} \frac{1}{|E_{k,\pm}|} \left[\eta_y \sin^2 k_y \pm \frac{1}{\tilde{E}_k} (\bar{\nu}^2 \eta_y \sin^2 k_y + 16 \xi^2 \eta_y \sin^4 k_y \sin^2 k_x) \right], \tag{A4}$$

$$\xi = \frac{4V_2}{N} \sum_{k,\pm} \frac{\sin^2 k_x}{|E_{k,\pm}|} \left[\xi \sin^2 k_y \pm \frac{1}{\tilde{E}_k} (\bar{\rho}^2 \xi \sin^2 k_y + 4\xi(\eta_x^2 \sin^2 k_x \sin^2 k_y + \eta_y^2 \sin^4 k_y) - \bar{\nu}\tilde{t} \eta_x \cos k_y \sin k_y) \right], \tag{A5}$$

$$\delta t = \frac{V_1}{N} \sum_{k,\pm} \frac{1}{|E_{k,\pm}|} \left[\tilde{t} (\cos^2 k_y + \cos^2 k_y) \pm \frac{1}{\tilde{E}_k} (2 \bar{\nu}^2 \tilde{t} \cos^2 k_y - 8 \bar{\nu} \tilde{t} \eta_x \xi \cos k_y \sin^2 k_x \sin k_y) \right], \tag{A6}$$

where

$$\tilde{E}_k = (\bar{\nu}^2 \bar{\rho}^2 + 4 \bar{\nu}^2 \tilde{t}^2 \cos^2 k_y - 32 \bar{\nu} \tilde{t} \eta_x \xi \cos k_y \sin^2 k_x \sin k_y + 4 \bar{\nu}^2 \eta_y^2 \sin^2 k_y + 16 \bar{\rho}^2 \xi^2 \sin^2 k_x \sin^2 k_y + 64 \xi^2 \sin^2 k_x \sin^2 k_y (\eta_x^2 \sin^2 k_x + \eta_y^2 \sin^2 k_y))^{1/2}. \tag{A7}$$

As mentioned above, the phase diagrams seen in Fig. 2 were mapped out by solving these equations self-consistently over the desired region of parameter space. That is to say, an initial set of mean-field values were substituted into the equations and then checked against the LHS of each equation. If the difference was greater than some tolerance set at

the beginning, the new values were fed back in until convergence was achieved.

2. Brillouin zone

The underlying bravais lattice is spanned by the primitive vectors $(3\mathbf{a}_1, 3\mathbf{a}_2) = (\mathbf{A}_1, \mathbf{A}_2)$ where $\mathbf{A}_1 = \frac{3}{2}(\sqrt{3}\hat{x} + \hat{y})a_0$, $\mathbf{A}_2 = 3\hat{y}a_0$ and a_0 is the lattice spacing. The reciprocal lattice vectors, $\mathbf{G}_1 = \frac{2\pi}{a_0}\frac{2}{3\sqrt{3}}\hat{x}$ and $\mathbf{G}_2 = \frac{2\pi}{a_0}\frac{1}{3\sqrt{3}}(\sqrt{3}\hat{y} - \hat{x})$, then follow and we have for the Brillouin zone

$$\mathbf{k} = m\mathbf{G}_1 + n\mathbf{G}_2 \quad m, n \epsilon \mathbb{N} = \frac{2\pi}{3\sqrt{3}a_0}\frac{1}{L}[(2m - n)\hat{x} + \sqrt{3}n\hat{y}]. \tag{A8}$$

Thus with $\mathbf{a}_1 = (-\frac{\sqrt{3}}{2}\hat{x} + \frac{1}{2}\hat{y})a_0$, $\mathbf{a}_2 = (\frac{\sqrt{3}}{2}\hat{x} + \frac{1}{2}\hat{y})a_0$, and $\mathbf{a}_3 = -\hat{y}a_0$ we get, $k_1 = \mathbf{a}_1 \cdot \mathbf{k} = \frac{2\pi}{3}\frac{n-m}{L}$, $k_2 = \mathbf{a}_2 \cdot \mathbf{k} = \frac{2\pi}{3}\frac{m}{L}$, and $k_3 = \mathbf{a}_3 \cdot \mathbf{k} = -\frac{2\pi}{3}\frac{n}{L}$.

[1] A. H. Castro Neto, F. Guinea, N. M. Peres, K. S. Novoselov, and A. K. Geim, Rev. Mod. Phys. **81**, 109 (2009).
[2] M. Berciu, T. G. Rappoport, and B. Janko, Nature (London) **435**, 71 (2005).
[3] S. Y. Zhou, G.-H. Gweon, A. V. Fedorov, P. N. First, W. A. de Heer, D.-H. Lee, F. Guinea, A. H. Castro Neto, and A. Lanzara, Nature Mater. **6**, 770 (2007).
[4] F. D. M. Haldane, Phys. Rev. Lett. **61**, 2015 (1988).
[5] S. Murakami, N. Nagaosa, and S.-C. Zhang, Phys. Rev. Lett. **93**, 156804 (2004).
[6] C. L. Kane and E. J. Mele, Phys. Rev. Lett. **95**, 146802 (2005).
[7] D. J. Thouless, M. Kohmoto, M. P. Nightingale, and M. den Nijs, Phys. Rev. Lett. **49**, 405 (1982).
[8] C. L. Kane and E. J. Mele, Phys. Rev. Lett. **95**, 226801 (2005).
[9] J. E. Moore and L. Balents, Phys. Rev. B **75**, 121306(R) (2007).
[10] B. A. Bernevig, T. L. Hughes, and S.-C. Zhang, Science **314**, 1757 (2006).
[11] M. König, S. Wiedmann, C. Brüne, A. Roth, H. Buhmann, L. W. Molenkamp, Xiao-Liang Qi, and Shou-Cheng Zhang, Science **318**, 766 (2007).
[12] R. Roy, Phys. Rev. B **79**, 195322 (2009).
[13] L. Fu, C. L. Kane, and E. J. Mele, Phys. Rev. Lett. **98**, 106803 (2007).
[14] C.-Y. Hou, C. Chamon, and C. Mudry, Phys. Rev. Lett. **98**, 186809 (2007).
[15] B. Seradjeh and M. Franz, Phys. Rev. Lett. **101**, 146401 (2008).
[16] S. Ryu, C. Mudry, C.-Y. Hou, and C. Chamon, Phys. Rev. B **80**, 205319 (2009).
[17] B. Seradjeh, C. Weeks, and M. Franz, Phys. Rev. B **77**, 033104 (2008).
[18] S. Raghu, X.-L. Qi, C. Honerkamp, and S.-C. Zhang, Phys. Rev. Lett. **100**, 156401 (2008).
[19] J. E. Drut and T. A. Lähde, Phys. Rev. Lett. **102**, 026802 (2009).
[20] X. Du, I. Skachko, F. Duerr, A. Luican, and E. Y. Andrei, Nature (London) **462**, 192 (2009).
[21] C.-Y. Hou, C. Chamon, and C. Mudry, arXiv:0909.2984 (unpublished).
[22] H.-M. Guo and M. Franz, Phys. Rev. B **80**, 113102 (2009).
[23] P. Mallet, F. Varchon, C. Naud, L. Magaud, C. Berger, and J.-Y. Veuillen, Phys. Rev. B **76**, 041403(R) (2007).
[24] T. Pereg-Barnea and A. H. MacDonald, Phys. Rev. B **78**, 014201 (2008) and references therein.